

PiaNet: A pyramid input augmented convolutional neural network for GGO detection in 3D lung CT scans

Weihua Liu^a, Xiabi Liu^{a*}, Xiongbiao Luo^b, Murong Wang^a, Guangyuan Zheng^a, Guanghui Han^c

^aBeijing Lab of Intelligent Information, School of Computer Science, Beijing Institute of Technology, Beijing.

Address: 5 South Zhongguancun Street, Haidian District, Beijing 100081, China

^bDepartment of computer science, Xiamen University, Xiamen

Address: No. 422, Siming South Road, Xiamen, Fujian 361005, China

^cSchool of Biomedical Engineering, Sun Yat-sen University, Guangzhou.

Address: No.132, Outer Ring Road East, University Town, Panyu District, Guangzhou 510006, China

Email: liuweihua@bit.edu.cn; liuxiabi@bit.edu.cn; xbluo@xmu.edu.cn; wangmurong@bit.edu.cn;

zhengguangyuan@bit.edu.cn; hangh3@mail.sysu.edu.cn;

Email of Corresponding authors: liuxiabi@bit.edu.cn.

Abstract: This paper proposes a new convolutional neural network with multiscale processing for detecting ground-glass opacity (GGO) nodules in 3D computed tomography (CT) images, which is referred to as PiaNet for short. PiaNet consists of a feature-extraction module and a prediction module. The former module is constructed by introducing pyramid multiscale source connections into a contracting-expanding structure. The latter module includes a bounding-box regressor and a classifier that are employed to simultaneously recognize GGO nodules and estimate bounding boxes at multiple scales. To train the proposed PiaNet, a two-stage transfer learning strategy is developed. In the first stage, the feature-extraction module is embedded into a classifier network that is trained on a large data set of GGO and non-GGO patches, which are generated by performing data augmentation from a small number of annotated CT scans. In the second stage, the pretrained feature-extraction module is loaded into PiaNet, and then PiaNet is fine-tuned using the annotated CT scans. We evaluate the proposed PiaNet on the LIDC-IDRI data set. The experimental results demonstrate that our method outperforms state-of-the-art counterparts, including the Subsolid CAD and Aidence systems and S4ND and GA-SSD methods. PiaNet achieves a sensitivity of 91.75% with only one false positive per scan.

Keywords: GGO Detection, Computer-Aided Detection (CAD), 3D CT images, convolutional neural networks

1. Introduction

Lung cancer is currently a leading cause of cancer death worldwide, accounting for more than 1.3 million deaths annually [1]. Early detection and treatment of lung cancer can improve the survival rate of patients. GGO is a highly vital sign of lung cancer at its early stage [2], which is defined as increased attenuation of the lung parenchyma without obscuration of the pulmonary vascular markings on the CT images [3]. However, due to their indistinct boundaries, unsharp appearance, and various sizes, GGO nodules are often overlooked by even experienced radiologists. A promising solution to this problem is the use of computer-aided detection techniques.

Although current automatic GGO detection methods have made significant progress, they still suffer from the three following problems: 1) they usually assume that the GGO appearance has predefined constraints on CT intensities or spherical shape, which yield unsatisfactory false positive rates, 2) they use hand-crafted visual features, which are sensitive to the high variability in the GGO appearance, and 3) they possibly fail to detect very small nodules or very large nodules.

Recently, deep networks have had an important role in medical healthcare [4, 5]. In this paper, we propose a new convolutional neural network named PiaNet for accurate GGO detection from 3D CT images. To address the multiscale problem of GGO nodules, we design PiaNet from the perspective of multiscale processing. PiaNet consists of a feature-extraction module and a prediction module to simultaneously extract the 3D boxes bounding GGO nodules and compute the corresponding classification confidence scores. We introduce pyramid multiscale source inputs into the feature-extraction module to prevent information loss at different scales. Furthermore, the skip connections are applied in the feature-extraction module to preserve the accurate location and multiscale information of detected objects, and the multiscale feature maps are employed in the prediction module to adapt to varied sizes of detected objects. To train our PiaNet with a small amount of annotated GGO data, we design a two-stage transfer learning method. Note that we cannot obtain a mass of annotated medical images for training deep networks, which is common in medical applications. In the first stage of our training, the feature-extraction module is solely trained by embedding it into a common classifier network and training this classifier network on a large data set of GGO and non-GGO patches, which are generated by performing data augmentation from a small data set of annotated CT images. In the second stage, the pretrained feature-extraction module is loaded into PiaNet, and the entire network is subsequently fine-tuned with a small number of annotated CT images. Data augmentation and hard negative mining are adopted in this stage to improve the generalization of training. To evaluate the effectiveness of our proposed PiaNet for GGO detection, we conduct GGO detection experiments on the LIDC-IDRI data set [6], which is the largest publicly available and most utilized

database of lung nodules.

Our main contributions are summarized as follows:

1) We present PiaNet, a deep convolutional neural network for GGO detection that is characterized by a contracting pathway with pyramid multiscale source connections, an expanding pathway with skip connections, and a prediction pathway with multiscale outputs for simultaneous computation of nodule location and classification. This network architecture is novel and demonstrates its value and rationality in ablation studies and comparison experiments. Although the skip connection and multiscale output are not our innovation, the whole architecture of this network can be regarded as our novelty.

2) We firstly introduce multiscale source connections in pyramid form into the neural network. In this way, we can not only reserve subtle locations of objects of interest, such as GGOs, in this paper but also address the problem of varied sizes of objects. As shown in our experiments, this strategy enables consistent gains of performance to different types of networks, including our PiaNet, SSD [20] and U-Net [23].

3) We design a two-stage transfer learning method to train our PiaNet using a small number of annotated CT images. Different from commonly employed transfer learning strategies that transfer the knowledge from other domains into the medical domain, we transfer the knowledge between different tasks in the same medical domain, between the discrimination of GGO/non-GGO regions from CT images and the detection of GGO regions from CT images. This two-stage transfer learning method leads to the outstanding performance of GGO detection on LIDC-IDRI data set. The resultant detection sensitivity is 91.75% at the rate of one false positive per scan, which to the best of our knowledge, is currently the best sensitivity.

The remainder of this paper is organized as follows: Section 2 surveys the related works. Section 3 and 4 presents our PiaNet architecture and its training method, respectively. Section 5 describes the implementation details and discuss experimental results. Section 6 provides some concluding remarks.

2. Related Work

2.1 Traditional GGO detection approaches

Traditional approaches to computer-aided GGO detection typically consist of two stages [7]: GGO candidate detection and false positive reduction, where hand-crafted image features are usually used. Bastawrous et al. [8] applied a Gabor filter to choose candidate GGOs and used an artificial neural network to reduce false positives. Zhou et al. [9] used cylinder filters suppressing vessels and noises to isolate GGO candidates and classified GGOs by boosting k -NN classifiers. Hyungseop et al. [10] extracted tentative regions using the binarization technique and classified the GGO nodules with a linear discriminant function. Jacobs et al. [11] first used intensity, shape, and texture features to describe candidates' appearance. Subsequently, they applied a linear discriminant classifier and a gentle boost classifier to classify candidate regions. They further introduced a novel set of contexture features and combined it with intensity, shape, and texture features for improving the classification performance [12].

2.2 Nodule detection based on deep learning

In recent years, nodule detection methods based on deep neural networks have achieved state-of-the-art detection performance, including GGO detection. Ginneken et al. [13] presented promising results of nodule extraction using an off-the-shelf convolutional neural network (CNN) that was pre-trained on a natural image recognition task. Setio et al. [14] used multiple CNNs to extract discriminative features from the candidates, and these features were used to classify candidates as nodules or non-nodule. Superior performance was achieved in the false positive reduction stage. Roth et al. [15] proposed an effective 2.5 D representation for lymph node detection by taking slices of the CT images from the point of interests in 3 orthogonal views. The slices were subsequently combined into a 3-channel image and processed by a deep network. Han et al. [16] proposed hybrid resampling in multi-CNN models for detecting 3D GGO nodules, which reduced the risk of missing small or large GGO nodules.

2.3 End-to-end network for object detection

The deep networks have achieved top accuracy on many challenging detection benchmarks of 2D natural images. They can be divided into two categories, two-stage methods and one-stage methods. Two-stage methods generate candidate bounding boxes and then classify candidates, such as Faster R-CNN [17] and Mask R-CNN [18]. One-stage methods combine candidate generation and classification as a whole, such as Yolo [19] and SSD [20]. More recently, the end-to-end networks have also been introduced to detect lung nodules in 3D CT images. Similar to Yolo method, Khosravan et al. [21] designed a single-scale 3D deep network architecture working in a single shot. Mat et al. [22] modified the SSD method and proposed GA-SSD that leverages the attention module with group convolutions based SSD method for lung nodule detection.

Our PiaNet belongs to the category of one-stage methods with an end-to-end network. Its structure is U-shape, including both encoder and decoder, while the only encoder exists in Yolo and SSD. U-shape architectures can also be found in U-Net [23] for medical image segmentation, recombination networks for facial keypoint localization [24], Feature Pyramid Networks(FPN) [25], and RetinaNet [26] for common object detection. The main difference between our PiaNet and other previous U-shape structures exists in the introduction of multiscale source connections and multiscale outputs.

2.4 Multi-task learning for medical images

In medical image analysis, researchers often simultaneously process several related tasks in multi-task learning ways to improve performance and generalization. Hussein et al. [27] proposed a 3D CNN-based network with a graph regularized sparse multi-task learning for risk stratification of lung nodules. Jie et al. [28] discussed a manifold regularized multi-task feature learning approach for multimodality disease classification to preserve both the intrinsic relatedness among multiple modalities of data and the data distribution information in each modality. In our paper, the GGO detection task divides into two interdependent sub-tasks: region location and region classification. These two sub-tasks are correlated with each other. We try to simultaneously extract the 3D boxes bounding GGO nodules and compute the corresponding classification confidence scores.

3. PiaNet Architecture

Due to GPU's memory limitation, the input of the PiaNet-based GGO nodule detection method is a CT cube with a fixed size ($128 \times 128 \times 128$ in our experiments). We preprocess CT images to meet this demand. Given a 3D CT volume, its voxel size is first normalized to $1 \times 1 \times 1 \text{ mm}^3$ using bilinear interpolation; then, the CT data in the Hounsfield unit is transformed to $[0, 255]$ by intensity normalization. GGOs must occur in the lung parenchyma, so lung parenchyma segmentation is performed. Finally, we divide the resultant volume into 3D cubes in a sliding-window way. Each cube will be inputted into our PiaNet to detect the GGOs in it. The final detection result is the combination of all the detected GGOs in each cube.

Fig.1 illustrates the architecture of our PiaNet, where a $128 \times 128 \times 128$ CT cube is inputted, and the consequent 47,616 (this number will be explained in this section) bounding boxes are generated and classified as GGOs or non-GGOs. As shown in Fig. 1, which contains three pathways: (i) a contracting pathway with source connections for injecting the multiscale source information for preventing source information loss at different scales; (ii) an expanding pathway with skip connections for combining low-level features and high-level semantics to preserve accurate location information and multiscale information of detected objects; and (iii) a prediction pathway that consists of a regressor and a classifier for making decisions on bounding boxes, where multiscale feature maps are utilized for adapting to varied sizes of objects. The contracting and expanding pathways are organized into the feature-extraction module, and the prediction pathway forms the multi-task prediction module.

The details of PiaNet are given in the following subsections.

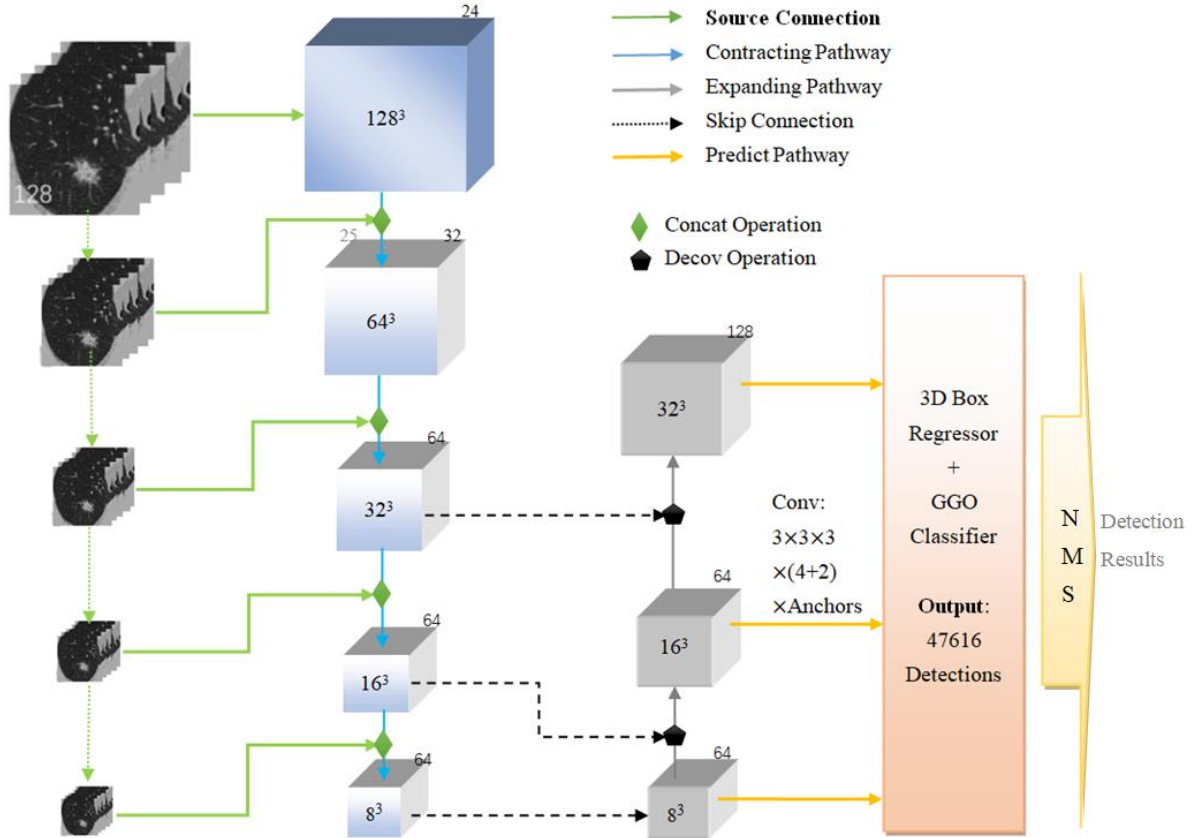


Fig. 1. The PiaNet architecture (the digits on the cube denote the corresponding numbers of channels.)

3.1 Contracting pathway with source connections

The contracting pathway is utilized to compute a feature hierarchy that consists of feature maps at several scales with a scaling step of 2. The pathway is composed of computation blocks (simplified as Conv blocks), each of which includes four operations of 3D convolution (Conv), batch normalization (BN), rectified linear units (ReLU), and max pooling (Max).

To capture the spatial information of GGOs at different scales, we construct a multiscale input structure by downsampling the source input with average pooling (Avg) and feeding it into each layer in the contracting pathway, as indicated by the green lines in Fig. 1. These connections are referred to source connections, with which we concatenate the Avg-pooled source image and feature map of the preceding block as the input of the next block. The green diamond icon in Fig. 1 shows this concatenation operation, which is simplified as "Concat Operation". Since source connections involve only one gray value at each spatial position, the block's width is increased only by one (e.g., from 24 to 25, as shown in the first block in Fig. 1).

The integrated computation of the two factors, i.e., computation block and source connection, is illustrated in Fig. 2, where the computation at the largest scale is taken as an example; the processing is the same for other scales.

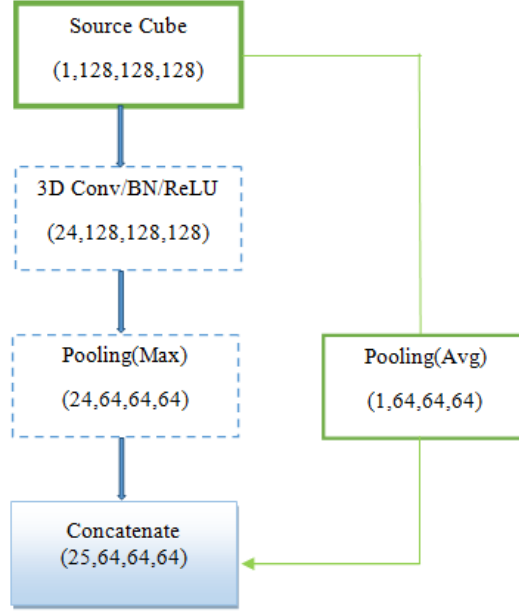


Fig. 2. Illustration of the concatenation computation of a computation block and the corresponding source connection, taking the first block of the contracting pathway in Fig. 1 as an example.

The average pooling of source images at various scales produces an image pyramid, as shown in Fig. 3. Thus by adding the source connections to the contracting pathway, the image pyramid can be blended into the network to achieve the ability of multiscale processing with a low-cost computation.

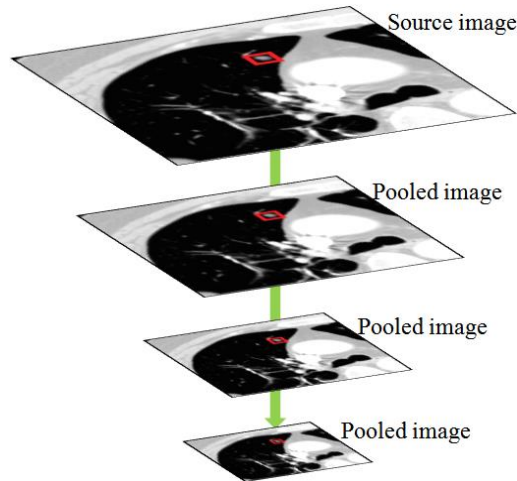


Fig. 3. Image pyramid that corresponds to our source connections

3.2 Expanding pathway with skip connections

The expanding pathway performs upsampling via Unpooling, Deconvolution, BN, and ReLU operations. Skip connections [29] are further applied to concatenate the feature maps from the contracting pathway with the output at the corresponding scale of the expanding pathway. In this way, we can preserve more subtle locations of GGOs in the final result.

By integrating an upsampling procedure and a skip connection, we obtain a deconvolution operation (simplified as Decov) in the expanding pathway; the detailed structure is illustrated in Fig. 4. We perform a $1 \times 1 \times 1$ convolution operation on the concatenation of the upsampled output from Unpooling-Deconvolution-BN-ReLU operations and the skipped result from the corresponding feature map in the contracting pathway to reduce the aliasing effect.

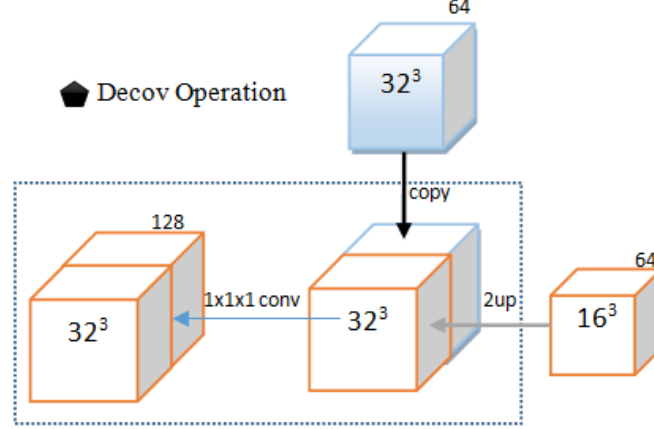


Fig. 4. Illustration of the structure of the Decov operation in the expanding pathway, which integrates the upsampled output and skipped information from the contracting pathway.

3.3 Prediction pathway

We detect the boxes bounding GGOs and simultaneously compute the corresponding classification confidence scores via the prediction pathway. To achieve this goal, we borrow the anchor box based idea from Faster R-CNN [17], which is introduced as follows.

The CT cube is first partitioned into predefined regular boxes, which are referred to as anchor boxes, that are simplified as anchors in the following descriptions. Each anchor will produce a resultant box with binary classification confidence scores, i.e., we have two types of outputs for each anchor.

To adapt to a varied size of GGOs, we consider multiscale processing that is reflected in two aspects. First, several scales in the expanding pathway are inputted into the prediction pathway and separately processed. For example, the blocks' outputs with scales of 8, 16, and 32 in the expanding pathway shown in Fig. 1 will be processed respectively and independently in the following prediction pathway. Second, multisize anchors are considered in the processing for each scale of feature maps, i.e., various sizes of anchors will be considered at each feature map's spatial location.

The structure of a prediction pathway for one scale of feature map (for example, 16) is illustrated in Fig. 5, where "Anchors' Sizes = 3" denotes that 3 different sizes of anchors are considered for this feature map. Since the size of this feature map is 16^3 , $16^3 \times 3$ anchors will be generated, based on which the same number of resultant boxes with classification confidence scores will be produced. The resultant box is a 3D square and is represented by a 4D vector (x, y, z, r) , where (x, y, z) is the 3D central point and r is the side length of the square. The corresponding classification confidence scores for GGO and non-GGO form a 2D vector. The convolution computation is performed on the feature map to obtain bounding boxes and classification scores for each anchor. Therefore, we need 3×6 convolutional kernels, in which 3×4 convolutional kernels are needed for bounding boxes and 3×2 convolutional kernels are needed for classification scores, as shown in the left part of Fig. 5 and the right part of Fig. 5, respectively. The shape of each convolutional kernel is $3^3 \times 64$, where 3^3 is the size of the kernel, and 64 is the number of channels in the feature map. Consequently, we will obtain $16^3 \times 3 = 12288$ 6D detection results for this scale of the feature map. As previously described, we perform the computation on various scales of feature maps, and the scales of 8, 16, and 32 are considered in our experiments. The number of anchor sizes in the feature maps with scales of 8, 16, and 32 are set to 5, 3, and 1, respectively. Thus, the number of total detection results for an inputted CT cube is $47,616 = 8^3 \times 5 + 16^3 \times 3 + 32^3 \times 1$ in this paper's experiments, as shown in Fig. 1.

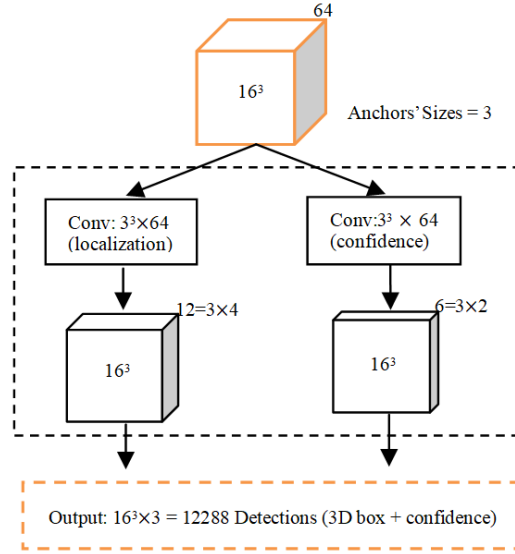


Fig. 5. Illustration of the prediction pathway for one scale of the feature map, i.e., the structure of the "3D box regressor + GGO classifier" block shown in Fig. 1.

After the resultant boxes and corresponding confidence scores are obtained from the prediction pathway, we perform nonmaximum suppression (NMS) to rule out the overlapping boxes. Among the overlapping boxes, only the box with the maximum confidence score will remain, and other boxes will be deleted. The remaining boxes will be designated GGOs if their classification confidence score is larger than a threshold or designated non-GGO otherwise. This threshold will be established in the applications.

4. Training

It is difficult to obtain a mass of annotated training data in medical image applications, which poses a challenge for deep neural network training. This dilemma is also encountered in this work. We can only obtain a small number of 3D CT scans with annotated GGO nodules. To solve the training of our PiaNet with a small amount of data, we develop a two-stage transfer learning method. First, we pretrain our feature-extraction module of PiaNet by embedding it in a GGO classifier network. This network is trained using a large data set of GGO and non-GGO patches that are generated from a small amount of annotated data and by using the data augmentation technique. Therefore, we use a large data set to learn the robust feature-extraction module for discriminating GGO patches from non-GGO patches in the first stage. Second, the pretrained feature-extraction module is integrated into PiaNet, and the whole network is further fine-tuned with a small data set, in which data augmentation and hard negative mining are adopted to improve the generalization of training. This two-stage learning strategy has excellent generalization ability, as demonstrated by our experimental results in Section 5.

We employ the data augmentation technique to transfer the knowledge between different tasks in the same medical domain, specifically, between the discrimination of GGO/non-GGO regions and the detection of GGO regions from CT images. This strategy differs from common transfer learning strategies that transfer knowledge from other domains to the medical domain. Zhou et al. [30] discovered that the gains of transfer learning among the same domain are significantly higher than those from different domains.

In our detection task, we need to locate the positions of GGOs in the image under the guidance of GGO classification and recognize whether the located regions are GGOs. We divide the detection task into these two subtasks and train the network in a multi-task learning way that simultaneously performs position location and region classification. The two subtasks can help each other improve their results. We discover that the features that describe the location and identify whether the region is a GGO are complementary and mutually reinforced in the trained network.

The details of data augmentation and our two-stage training method are discussed in the following section.

4.1 Data augmentation

Data augmentation is a feasible solution to solve the problem of small data training by automatically generating more data from the original small data set. We apply the main data augmentation operations to our problem, including flipping, resizing, translating, rotating, and swapping.

- 1) Flipping: 3D images are randomly flipped with respect to three orthogonal dimensions (coronal, sagittal, and axial).
- 2) Resizing: 3D images are randomly resized with the ratio in $[0.9, 1.1]$.
- 3) Translating: 3D images are randomly translated lightly in three axes.
- 4) Rotating: 3D images are randomly rotated by small degrees.
- 5) Swapping: 3D images are generated by randomly reordering the values in three axes.

4.2 First-stage training

In this stage, the feature-extraction module in PiaNet is joined with an average pooling layer and a two-class softmax layer to construct a GGO classifier for classifying a 3D CT region as GGO or non-GGO. This classifier is trained with a large data set that is generated as follows: First, positive GGO patches and negative non-GGO patches are cropped from a small number of annotated lung CT scans. Second, more positive patches are generated by performing the five operations of data augmentation. Using this large data set of GGO and non-GGO patches, the classifier network is trained by minimizing the softmax-loss function with stochastic gradient descent (SGD). To avoid slow convergence, the weights are initialized with the Xavier initialization method [31]. After the training is completed, we obtain the feature-extraction module of our PiaNet. Since the classifier network only involves a binary classification problem and the size of the patches inputted into the classifier network is only 1/8 of the inputted CT cubes of the whole PiaNet, the classifier can be trained quickly to produce an acceptable initial feature-extraction module for more effective training of the whole PiaNet.

4.3 Second-stage Training

In this stage, the pretrained feature-extraction module is loaded into PiaNet and further trained with a multi-task learning method. As described in Section 3.3, we attempt to regress from the anchors to the corresponding ground-truth boxes and classify them into GGOs or non-GGOs. These two objectives are combined as a single multi-task objective for training PiaNet.

Formally, let $\Pi_{ij} = \{1, 0\}$ be an indicator that matches the i -th anchor (denoted as a) with the j -th ground truth box (denoted as g) in the training data, which is determined according to the intersection over union (IoU) values between the anchors and the ground-truth boxes. Each ground-truth box will be matched with the anchor with its maximum IoU value. Let c be the outputted classification confidence scores, let l be the outputted bounding boxes, and let g be the ground-truth bounding boxes. The multi-task loss function is defined as

$$L(\Pi, c, l, g) = L_{conf}(\Pi, c) + \alpha L_{loc}(\Pi, l, g), \quad (1)$$

where L_{conf} is the loss for the classification confidence, L_{loc} is the loss for the resultant box, and α is the balancing of the contribution of two loss terms and is set to 1 by cross-validation experiments in this paper.

The loss for classification confidence is defined as the binary cross-entropy loss over the confidences of the two classes:

$$L_{conf}(\Pi, c) = - \sum_{i, \Pi_{ij}=1} \log(c_j) - (1 - c_j) \sum_{i, \Pi_{ij}=0} \log(1 - c_j). \quad (2)$$

Regarding the loss for the resultant box, the modified smooth $L1$ loss [32] between l and g is employed. Let (x, y, z, r) be the representation of a box, as described in Section 3.3. Let t_j^k ($k \in \{x, y, z\}$) and p_j^k ($k \in \{x, y, z\}$) be the k -th coordinate of center point of the j -th ground-truth box and the j -th predicted resultant box, respectively, and let t_j^r and p_j^r be the side length of the j -th ground-truth box and the j -th computed box, respectively. We have

$$L_{loc}(\Pi, l, g) = \sum_{i, j} \Pi_{ij} (\beta \sum_{k \in \{x, y, z\}} \text{Smooth}_{L1}(t_j^k - p_j^k) + (1 - \beta) \text{Smooth}_{L1}(t_j^r - p_j^r)), \quad (3)$$

where the smooth $L1$ function is defined as

$$\text{Smooth}_{L1}(x) = \begin{cases} 0.5x^2, & \text{if } |x| < 1 \\ |x| - 0.5, & \text{otherwise} \end{cases}. \quad (4)$$

The weight term β is set to 0.6 via careful experiments in this paper, which means that we pay more attention to the center points of the bounding boxes than their side length.

The positions and sizes of both the ground-truth boxes and computed boxes are measured based on the anchors. Let a_i^k ($k \in \{x, y, z\}$) be the k -th coordinate of the center point of the i -th anchor, and let a_i^r be the side length of the i -th anchor. Subsequently, t_j^k ($k \in \{x, y, z\}$), p_j^k ($k \in \{x, y, z\}$), t_j^r , and p_j^r in Eq. 3 are computed as

$$t_j^k = (g_j^k - a_i^k) / a_i^r, \quad (5)$$

$$p_j^k = (l_j^k - a_i^k) / a_i^r, \quad (6)$$

$$t_j^r = \log(g_j^r / a_i^r), \quad (7)$$

$$p_j^r = \log(l_j^r / a_i^r), \quad (8)$$

respectively.

Our multi-task learning is performed with training data to minimize Eq. (1) by using the SGD algorithm. The training data in this stage are collected as follows: First, GGO patches are randomly cropped from the annotated lung scans. These patches are augmented by using the flipping and resizing operations described in Section 4.1. Actually, the remaining 3 data augmentation operations are also tested here but fail to show significant improvement. Second, we adopt a hard negative mining technique [33] to solve the class unbalance problem, in which the number of negative patches is substantially greater than that of positive patches in the detection. This hard negative mining is performed in three steps. First, all the CT cubes in the training data set are processed by PiaNet to obtain tens of thousands of detections, each of which is associated with a resultant box and a classification confidence score. Second, initial negative examples are randomly selected from these boxes, where the number of selected examples is determined by experience. Third, all the selected negative examples are sorted in descending order of their confidence scores, and the top K examples are chosen as the final negative examples that are employed in training. In this way, the number of negative examples and that of positive examples will be balanced, and hard negative examples will be selected to improve the training.

5. Experiments

In this section, we first describe the experimental setup and implementation details of PiaNet. Second we report the results of two groups of experiments. The first group of experiments is conducted to evaluate the roles of PiaNet components, compared with classical networks including U-Net and SSD. The second group of experiments is conducted to test the overall performance of PiaNet and compare it with that of other counterparts, including two state-of-the-art methods and two CAD systems. All experiments were conducted on a computer with four NVIDIA GeForce TITAN Xp GPUs.

5.1 Experimental Setup

5.1.1 Data set

The data set is collected from the largest publicly available database of lung nodules, the LIDC-IDRI data set [6]. The data set contains 1018 CT scans and XML-based annotations to stimulate the development of CAD methods for lung nodule detection, classification, and quantitative assessment. Each scan was annotated by 4 experienced thoracic radiologists using a two-phase reading process. Following Naidich et al. [34], we discarded scans with slice thicknesses greater than 3 mm, considering 3D detection in this paper. Scans with inconsistent slice spacing or missing slices can be considered noise and were also excluded. The annotated nodules in the LIDC-IDRI data set are categorized based on the morphological characteristics and are scored by the radiologists using a 5-point score. Only nodules with scores less than 5 are considered real GGOs and selected for our experiments. Furthermore, we only considered the nodules that are recognized by the majority of the radiologists, at least 3 of 4 radiologists. The GGO nodules that remain after the processing are the targets that the algorithms should detect. Other excluded GGO nodules are labeled "irrelevant findings" and are not selected as true positives or false positives to alleviate the problem of disagreement regarding the definition of a GGO nodule. This strategy is also adopted in the LUNA16 Challenge [35].

A total of 302 CT scans from 299 patients were collected from the LIDC-IDRI data set, in which 635 GGO nodules (271 nodules recognized by 3 radiologists and 364 nodules recognized by 4 radiologists) were included. The diameter of the nodules varies from 3 to 34 mm, with a median of 10.3 mm. We use 250 scans in these 302 scans as the training set and use the remaining 52 scans as the test set.

For one 3D CT scan, we can produce dozens of $128 \times 128 \times 128$ cubes. For example, the size of one CT scan is $512 \times 512 \times 206$. After preprocessing with voxel size normalization, intensity normalization, and lung parenchyma segmentation, as described in the first paragraph of Section 3, the size of the processed scan is reduced to $252 \times 222 \times 192$. This 3D CT volume is divided into $128 \times 128 \times 128$ cubes in a sliding-window way, where the stride is set to 64. Consequently, we produced 24 cubes for this CT scan. Note that the roughly labeled lung parenchyma for each scan is mainly provided in the LUNA 16 challenge, which is obtained using an automatic lung segmentation algorithm [36]. For some scans unseen in the LUNA 16 challenge, we manually segmented the lung parenchyma.

5.1.2 Evaluation criteria

In our experiments, we perform a free-response receiver operating characteristic (FROC) analysis [37] to evaluate the performance of GGO detection. The sensitivity and false positives are extensively utilized for evaluating the detection performance. The sensitivity is defined as the fraction of detected true positives divided by the number of all true nodules. The FROC curve reflects the relationship between the sensitivity and the false positives per scan (FPs/scan), in which the sensitivity is plotted as a function of the average number of false positives per scan (FPs/scan). The overall evaluation from the FROC curve is measured as the average of the sensitivity at seven predefined FPs/scan: 1/8, 1/4, 1/2, 1, 2, 4, and 8. This performance metric was introduced into the ANODE09 Challenge and referred to as the competition performance metric (CPM) [38].

5.1.3 Network configuration

Table 1 summarizes the detailed configuration of PiaNet, which is applied in the experiments. We have the following description from Table 1: 1) in the contracting pathway, five Conv-BN-ReLU-Pooling blocks with source connections are constructed; 2) in

the expanding pathway, only three layers are constructed due to the GPU memory limitation. Additionally, due to this issue, we have to control the output size in this pathway. Therefore, although we expect an output shape of (128, 16, 16, 16) when expanding from the scale of 8 to 16, we can only produce the output with the shape of (64, 16, 16, 16) in practice, as shown in Fig. 1; and 3) in the prediction pathway, 3×3×3 convolutions are applied to both the bounding box regressor and the GGO classifier. All the scales of information decoded in the expanding pathway, including 32×32×32, 16×16×16, and 8×8×8, are employed and inputted into the prediction pathway. The number of anchor sizes are set to 1, 3, and 5 for these three scales, which lead to a total of 9 anchor sizes: 4, 6, 8, 10, 12, 16, 20, 26, and 32 mm. Their details are listed in Table 2. To sum up, we will generate 47,616 ($=32^3 \times 1 + 16^3 \times 3 + 8^3 \times 5$) anchors for each CT cube, based on which 47,616 resultant boxes and their classification confidence scores will be computed.

Table 1: PiaNet configuration used in the experiments (OP: operation)

| | <i>Layer Number</i> | <i>Name</i> | <i>Output Shape</i> |
|---------------------|---------------------|--------------------------|------------------------------|
| Source | 0 | Input | (1, 128,128,128) |
| Contracting pathway | 1 | Conv block | (24, 64,64,64) |
| | 2 | Concat OP | (25,64,64,64) |
| | 3 | Conv block | (32,32,32,32) |
| | 4 | Concat OP | (33,32,32,32) |
| | 5 | Conv block | (64,16,16,16) |
| | 6 | Concat OP | (65,16,16,16) |
| | 7 | Conv block | (64,8,8,8) |
| | 8 | Concat OP | (65,8,8,8) |
| | 9 | Conv block (No Pooling) | (64,8,8,8) |
| Expanding pathway | 10 | 1x1x1Conv | (64,8,8,8) |
| | 11 | Decov OP | (64,16,16,16) |
| | 12 | Decov OP | (128,32,32,32) |
| Prediction pathway | 13 | BoxRegressor/ Classifier | (4,32,32,32)/ (2,32,32,32) |
| | 14 | BoxRegressor/ Classifier | (12,16,16,16)/ (6,16,16,16) |
| | 15 | BoxRegressor/ Classifier | (20,8,8,8)/ (10,8,8,8) |
| Detection | 16 | Output | (47616,4,1,1)/ (47616,2,1,1) |

Table2. Configuration of anchors' sizes for each scale of decoded feature maps (#: the number of its)

| <i>Feature map</i> | <i># anchor size</i> | <i># anchor box</i> | <i>Size (mm)</i> | | | | |
|--------------------|----------------------|---------------------|------------------|-----------|----|----|----|
| 32×32×32 | 1 | 32768 | 4 | \ | \ | \ | \ |
| 16×16×16 | 3 | 12288 | 6 | 8 | 10 | \ | \ |
| 8×8×8 | 5 | 2560 | 12 | 16 | 20 | 26 | 32 |
| Sum | | 47616 | | | | | |

5.2 Experimental Results

5.2.1 Ablation experiments

Different from other network structures for object detection, our network architecture is designed on the basis of the idea of multiscale processing, which is realized in the combination of three strategies. First, pyramid multiscale source connections are introduced into the contracting pathway to prevent source information loss at different scales. Second, the expanding pathway with skip connections is adopted for preserving the accurate location and multiscale information of detected objects. Third, the use of multiscale feature maps in the prediction pathway contributes the robustness to varied sizes of objects. We conduct controlled experiments to examine how each of these three strategies affects performance. For all the experiments, we use the same training data set and data augmentation operations; the hyperparameters of the network are also shared.

If the source connections are disregarded, then our PiaNet is closely related to SSD [20] and U-Net [23]. SSD is a popular single-shot detector for natural images, which produces predictions from multiscale feature maps, but only in the contracting pathway. Conversely, U-Net has an elegant contracting-expanding structure, but it only uses the last feature map in the prediction and disregards the multiscale processing.

To show the importance of introducing the source connections into the networks, we conduct six experiments of GGO detection with or without source connections based on PiaNet, SSD and U-Net. Table 3 lists the results of these experiments, which shows

that source connections improve the sensitivity from 78.2% to 83.7% for SSD, from 82.4% to 86.9% for U-Net, and from 87.3% to 94.2% for PiaNet, all at a slightly better FPs/scan rate. The maximal boosted performance reaches 6.9 points. The important observation is that the gains with our source connections are consistent among different networks.

Table 3 also shows that our expanding pathway and multiscale prediction has an important role in improving the performance. To understand the importance of the expanding pathway, we can compare the performance of SSD and PiaNet(-). The main difference between them is whether the expanding pathway is utilized. We observe that the sensitivity is improved from 78.2% of SSD without an expanding pathway to 87.3% of PiaNet(-) with an expanding pathway. Note that some methods that have been improved by adding an expanding pathway in the SSD have been proposed, such as the method by Fu et al. [39], which has an encoder-decoder structure, similar to PiaNet without source connections, i.e., PiaNet(-). By comparing PiaNet(-) with PiaNet, we discover that our source connections make our network significantly surpass these type of SSD extended methods. For the importance of multiscale prediction, we can compare the performance of U-Net and PiaNet(-) and determine that the sensitivity is improved from 82.4% of U-Net without multiscale prediction to 87.3% of PiaNet(-) with multiscale prediction.

Table 3. GGO detection results using SSD, U-Net, and PiaNet (+: with source connections, -: without source connections)

| <i>Methods</i> | <i>Multiscale feature maps?</i> | <i>Expanding pathway?</i> | <i>Source connection?</i> | <i>Sensitivity</i> | <i>FPS/scan</i> |
|-------------------|---------------------------------|---------------------------|---------------------------|--------------------|-----------------|
| (a) SSD | Y | / | N | 78.2% | 9.1 |
| (b) SSD(+) | Y | / | Y | 83.7% | 8.9 |
| (c) U-Net | / | Y | N | 82.4% | 7.8 |
| (d) U-Net(+) | / | Y | Y | 86.9% | 7.7 |
| (e) PiaNet(-) | Y | Y | N | 87.3% | 8.5 |
| (f) PiaNet | Y | Y | Y | 94.2% | 6.7 |

To further evaluate the effect of using multiscale feature maps for prediction, we progressively remove feature maps and observe the change in performance. Table 4 shows a stable decrease in accuracy, from 94.2% to 90.3%, with a reduction in the feature map scales. The findings show that we need sufficient scales to cover the wide range of GGOs' sizes.

Table 4. Effects of using multiscale feature maps

| <i>Prediction from features maps:</i> | | | <i>Anchor box</i> | <i>Performance</i> | |
|---------------------------------------|--------------------------|-----------------------|-------------------|--------------------|----------|
| $32 \times 32 \times 32$ | $16 \times 16 \times 16$ | $8 \times 8 \times 8$ | #number | Sensitivity | FPS/scan |
| Y | Y | Y | 47616 | 94.2% | 6.7 |
| Y | Y | \ | 45056 | 92.5% | 6.8 |
| Y | \ | \ | 32768 | 90.3% | 7.1 |

Table 3 reveals that our PiaNet achieves the highest sensitivity (94.2%) at the lowest FPs/scan rate (6.7) among these detection experiments, which demonstrates the superiority of our network architecture to U-Net and SSD.

5.2.2 Comparison experiments

In this section, we compare the GGO detection performance of our PiaNet with two state-of-the-art methods, GA-SSD [22] and S4ND [21], and two real CAD systems, SubsolidCAD [12] and Aidence [40]. GA-SSD is an improved method that is based on SSD by implementing the attention mechanism and the group convolution, and the S4ND method is a single-shot and single-scale method. SubsolidCAD is a conventional system that uses 4 categories of hand-crafted features to describe the appearance of GGOs. The system focuses on GGO nodule detection and can reach a sensitivity of 80% at an average rate of one false positive per scan; the corresponding CPM value is 0.734. The Aidence system is based on convolutional networks, which were trained on a subset of studies from the National Lung Screening Trial [41] and achieved the best CPM of 0.764 in the LUNA16 Challenge [40]. The LUNA16 challenge data set contains 253 GGO nodules from the LIDC-IDRI data set. All of the nodules are contained in our experimental data.

Fig. 6 compares the performance of GA-SSD, S4ND, Subsolid CAD, Aidence system, and PiaNet. The findings show that PiaNet outperforms other methods. Our method achieves a CMP of 0.8826, which is better than a CMP of 0.8547 achieved by the GA-SSD, a CMP of 0.8666 achieved by S4ND, a CMP of 0.734 achieved by the SubsolidCAD system, and a CMP of 0.767 achieved by the Aidence system. The corresponding performance increases for GA-SSD, S4ND, SubsolidCAD and Aidence are 3.26%, 1.85%, 20.25% and 15.07%, respectively.

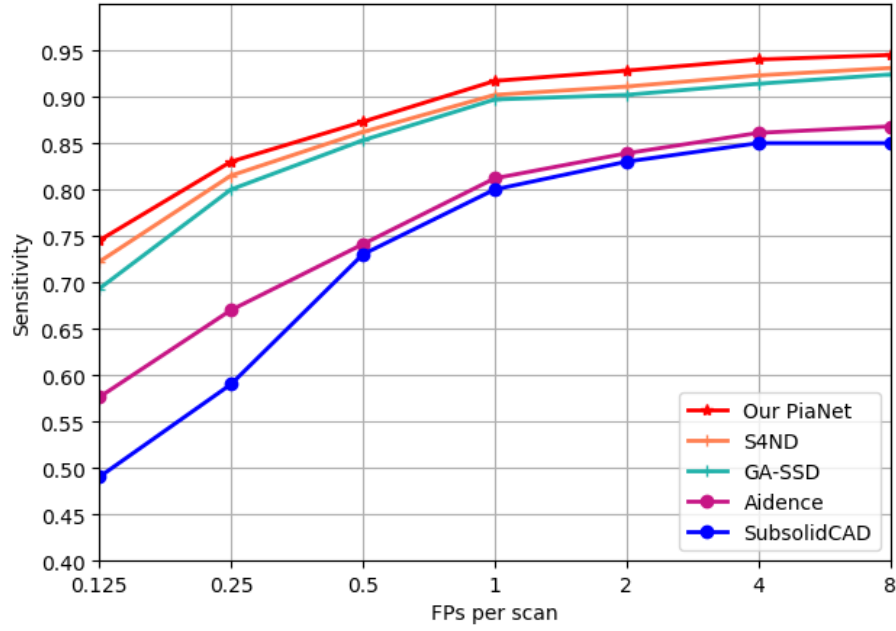


Fig. 6. Comparison of performance from our PiaNet, GA-SSD, S4ND, SubsolidCAD and Aidence.

5.3 Detection Visualization

In Fig. 7, we visualize the detection results, including the correct ones, and a few errors, which are produced from PiaNet by establishing the threshold of confidence scores for recognizing GGO to be 0.8. These example results demonstrate that PiaNet is robust, and can identify GGO nodules with varied sizes (from 3 mm to 33 mm in our test set) and irregular shapes and textures.

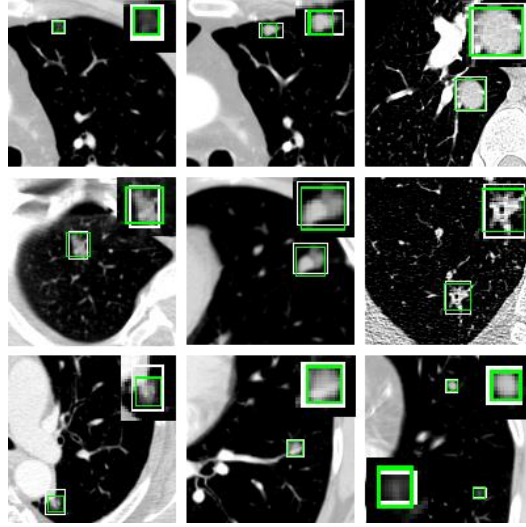


Fig. 7. Examples of correct detections by PiaNet on the LIDC-IDRI data set, where the white rectangles denote the ground-truth boxes and the green rectangles denote the detection results, and the detected nodules are zoomed at the top-right area.

Examples of missed GGO nodules (false negatives) and false-detected results (false positives) by PiaNet are shown in the top row of Fig.8 and bottom row of Fig. 8, respectively. We can see that the missed nodules are notably low in contrast or very uncommon, and the false-detected nodules are usually located very close to the other tissues with a similar appearance, such as blood and chest wall. To address these hard cases to further reduce the error rate, more discriminative features should be learned by making the network training focus on hard examples.

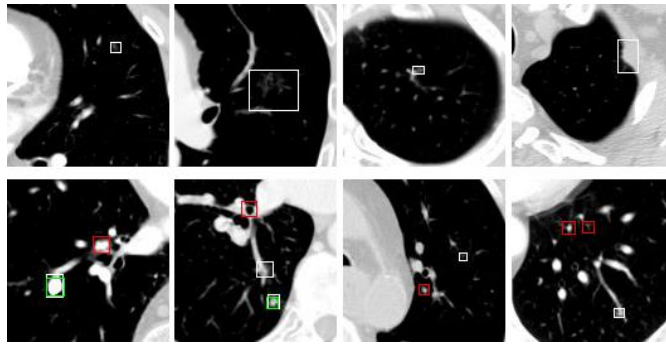


Fig.8. Examples of missing results (false negatives, shown in the top row) and false-detected results (false positives, shown in the bottom row) by PiaNet on the LIDC-IDRI data set, where the white rectangles denote the ground-truth boxes; the green rectangles denote the right results; and the red rectangles denote the wrong results.

6. Conclusions

In this paper, we have proposed a new convolutional neural network for detecting GGO nodules in 3D CT scans, which is named PiaNet. PiaNet is designed based on the idea of multiscale processing for addressing the problem of varied sizes of GGOs. PiaNet is composed of a feature-extraction module including a contracting pathway with pyramid multiscale source connections and an expanding pathway with skip connections, and a prediction module with multiscale outputs. Through the introduction of source connections and the integrated adoption of three multiscale processing strategies, PiaNet achieves satisfactory performance. PiaNet substantially and stably outperforms the state-of-the-art counterparts, including two methods, S4ND and GA-SSD, and two real systems, Subsolid CAD and Aidence. The improvements in the CPM values compared with those obtained with these found counterparts are 3.26%, 1.85%, 20.25% and 15.07%, respectively. The ablation studies further justify the effectiveness of each of the three multiscale processing strategies. From these experimental results, we believe that PiaNet offers a promising tool for GGO nodule detection in the clinical diagnosis of lung cancer.

Although PiaNet can detect the majority of nodules with different sizes and irregular shapes and textures, it still misses some very uncommon nodules and some nodules with very low contrast and incurs false-detected nodules that are located very close to other tissues with similar appearances. It may be helpful to further reduce the error rate by making the network training focus on the hard examples. We plan to explore this approach in future studies.

Funding: This work was supported by the National Natural Science Foundation of China [grant numbers 60973059, 81171407, 61901533]; Program for New Century Excellent Talents in University of China [grant number NCET-10-0044];

Declaration of competing interest: All co-authors of this manuscript confirm that there are no financial or personal relationships with any people or organizations that could inappropriately influence the actions of any author of this manuscript.

REFERENCES

- [1] R. Siegel, J. Ma, Z. Zou *et al.*, "Cancer statistics, 2014," *Ca A Cancer Journal for Clinicians*, vol. 65, no. 1, pp. 5-29, 2015.
- [2] C. I. Henschke, D. F. Yankelevitz, R. Mirtcheva *et al.*, "CT screening for lung cancer: frequency and significance of part-solid and nonsolid nodules," *Ajr American Journal of Roentgenology*, vol. 178, no. 5, pp. 1053, 2002.
- [3] M. W. Jr, and R. M. Shah, "Isolated diffuse ground-glass opacity in thoracic CT: causes and clinical presentations," *Ajr American Journal of Roentgenology*, vol. 184, no. 2, pp. 613, 2005.
- [4] M. Z. Uddin, and M. M. Hassan, "Activity recognition for cognitive assistance using body sensors data and deep convolutional neural network," *IEEE Sensors Journal*, 2018.
- [5] M. Z. Uddin, M. M. Hassan, A. Alsanad *et al.*, "A body sensor data fusion and deep recurrent neural network-based behavior recognition approach for robust healthcare," *Information Fusion*, vol. 55, pp. 105-115, 2020.
- [6] A. S. 3Rd, G. McLennan, L. Bidaut *et al.*, "The Lung Image Database Consortium (LIDC) and Image Database Resource Initiative (IDRI): a completed reference database of lung nodules on CT scans," *Medical Physics*, vol. 38, no. 2, pp. 915, 2011.
- [7] L. Linying, L. Xiabi, Z. Chunwu *et al.*, "A Review of Ground Glass Opacity Detection Methods in Lung CT Images," *Current Medical Imaging Reviews*, vol. 12, no. 999, pp. 1-1, 2017.
- [8] H. A. Bastawrous, T. Fukumoto, M. Tsudagawa *et al.*, "Detection of ground glass opacities in lung CT images using Gabor filters and neural networks," *IEEE Instrumentation and Measurement Technology Conference Proceedings*, pp. 251-256, 2005.
- [9] J. Zhou, S. Chang, D. N. Metaxas *et al.*, "Automatic Detection and Segmentation of Ground Glass Opacity Nodules," *Lecture Notes in Computer Science*, vol. 9, no. Pt 1, pp. 784-91, 2006.
- [10] H. Kim, T. Nakashima, Y. Itai *et al.*, "Automatic detection of ground glass opacity from the thoracic MDCT images by using density features," *International Conference on Control, Automation and Systems*, pp. 1274-1277, 2007.
- [11] C. Jacobs, C. I. Sánchez, S. C. Saur *et al.*, "Computer-aided detection of ground glass nodules in thoracic CT images using shape, intensity and context features," *International conference on medical image computing and computer-assisted intervention*, pp. 207-214, 2011.
- [12] C. Jacobs, E. M. van Rikxoort, T. Twellmann *et al.*, "Automatic detection of subsolid pulmonary nodules in thoracic computed tomography images," *Medical image analysis*, vol. 18, no. 2, pp. 374-384, 2014.

- [13] B. Van Ginneken, A. A. Setio, C. Jacobs *et al.*, "Off-the-shelf convolutional neural network features for pulmonary nodule detection in computed tomography scans," *IEEE 12th International symposium on biomedical imaging (ISBI)*, pp. 286-289, 2015.
- [14] A. A. A. Setio, F. Ciompi, G. Litjens *et al.*, "Pulmonary nodule detection in CT images: false positive reduction using multi-view convolutional networks," *IEEE transactions on medical imaging*, vol. 35, no. 5, pp. 1160-1169, 2016.
- [15] H. R. Roth, L. Lu, A. Seff *et al.*, "A new 2.5 D representation for lymph node detection using random sets of deep convolutional neural network observations," *International conference on medical image computing and computer-assisted intervention*, pp. 520-527, 2014.
- [16] G. Han, X. Liu, G. Zheng *et al.*, "Automatic recognition of 3D GGO CT imaging signs through the fusion of hybrid resampling and layer-wise fine-tuning CNNs," *Medical & biological engineering & computing*, pp. 1-12, 2018.
- [17] S. Ren, K. He, R. Girshick *et al.*, "Faster R-CNN: Towards Real-Time Object Detection with Region Proposal Networks," *IEEE Trans Pattern Anal Mach Intell*, vol. 39, no. 6, pp. 1137-1149, 2017.
- [18] K. He, G. Gkioxari, P. Dollár *et al.*, "Mask R-CNN," *Proceedings of the IEEE international conference on computer vision*, pp. 2980-2988, 2017.
- [19] J. Redmon, S. Divvala, R. Girshick *et al.*, "You Only Look Once: Unified, Real-Time Object Detection," *Proceedings of the IEEE conference on computer vision and pattern recognition*, pp. 779-788, 2016.
- [20] W. Liu, D. Anguelov, D. Erhan *et al.*, "SSD: Single Shot MultiBox Detector," *European Conference on Computer Vision*, pp. 21-37.
- [21] N. a. B. Khosravan, Ulas, "S4ND: Single-Shot Single-Scale Lung Nodule Detection," *International Conference on Medical Image Computing and Computer-Assisted Intervention*, pp. 794-802, 2018.
- [22] J. Ma, X. Li, H. Li *et al.*, "Group-Attention Single-Shot Detector (GA-SSD): Finding Pulmonary Nodules in Large-Scale CT Images," *arXiv preprint arXiv:1812.07166*, 2018.
- [23] O. Ronneberger, P. Fischer, and T. Brox, "U-Net: Convolutional Networks for Biomedical Image Segmentation," *International Conference on Medical Image Computing and Computer-Assisted Intervention*, pp. 234-241, 2015.
- [24] S. Honari, J. Yosinski, P. Vincent *et al.*, "Recombinator networks: Learning coarse-to-fine feature aggregation," *Proceedings of the IEEE Conference on Computer Vision and Pattern Recognition*, pp. 5743-5752, 2016.
- [25] T. Y. Lin, P. Dollár, R. Girshick *et al.*, "Feature Pyramid Networks for Object Detection," *Proceedings of the IEEE conference on computer vision and pattern recognition*, pp. 2117-2125, 2017.
- [26] T. Y. Lin, P. Goyal, R. Girshick *et al.*, "Focal Loss for Dense Object Detection," *IEEE Transactions on Pattern Analysis & Machine Intelligence*, vol. PP, no. 99, pp. 2999-3007, 2017.
- [27] S. Hussein, K. Cao, Q. Song *et al.*, "Risk stratification of lung nodules using 3d cnn-based multi-task learning," *International conference on information processing in medical imaging*, pp. 249-260, 2017.
- [28] B. Jie, D. Zhang, B. Cheng *et al.*, "Manifold regularized multitask feature learning for multimodality disease classification," *Human brain mapping*, vol. 36, no. 2, pp. 489-507, 2015.
- [29] C. Bishop, and C. M. Bishop, *Neural networks for pattern recognition*: Oxford university press, 1995.
- [30] H.-Y. Zhou, A. Oliver, J. Wu *et al.*, "When Semi-Supervised Learning Meets Transfer Learning: Training Strategies, Models and Datasets," *arXiv preprint arXiv:1812.05313*, 2018.
- [31] X. Glorot, and Y. Bengio, "Understanding the difficulty of training deep feedforward neural networks," *Journal of Machine Learning Research*, vol. 9, pp. 249-256, 2010.
- [32] R. Girshick, "Fast R-CNN," *Computer Science*, 2015.
- [33] A. Shrivastava, A. Gupta, and R. Girshick, "Training region-based object detectors with online hard example mining," *Proceedings of the IEEE Conference on Computer Vision and Pattern Recognition*, pp. 761-769, 2016.
- [34] D. P. Naidich, A. A. Bankier, H. Macmahon *et al.*, "Recommendations for the management of subsolid pulmonary nodules detected at CT: a statement from the Fleischner Society," *Radiology*, vol. 266, no. 1, pp. 304-317, 2013.
- [35] LUNA16. "Lung nodule analysis 2016," <https://luna16.grand-challenge.org/>.
- [36] E. M. Van Rikxoort, B. De Hoop, M. A. Viergever *et al.*, "Automatic lung segmentation from thoracic computed tomography scans using a hybrid approach with error detection," *Medical Physics*, vol. 36, no. 7, pp. 2934-2947, 2009.
- [37] H. L. Kundel, K. S. Berbaum, and D. D. Dorfman, "Receiver Operating Characteristic Analysis in Medical Imaging," *Journal of the Icru*, 2008.
- [38] M. Niemeijer, M. Loog, M. D. Abramoff *et al.*, "On combining computer-aided detection systems," *IEEE Transactions on Medical Imaging*, vol. 30, no. 2, pp. 215-23, 2011.
- [39] C. Y. Fu, W. Liu, A. Ranga *et al.*, "DSSD : Deconvolutional Single Shot Detector," *arXiv preprint arXiv:1701.06659*, 2017.
- [40] S. Aaa, A. Traverso, B. T. De *et al.*, "Validation, comparison, and combination of algorithms for automatic detection of pulmonary nodules in computed tomography images: The LUNA16 challenge," *Medical Image Analysis*, vol. 42, pp. 1-13, 2016.
- [41] C. S. White, "National Lung Screening Trial," *Journal of Thoracic Imaging*, vol. 26, no. 2, pp. 86-87, 2011.